Salicylic acid-mediated plasmodesmal closure via Remorin-dependent lipid organization

Dingquan Huang[a,b,1], Yanbiao Sun[a,b,1], Zhiming Ma[c,1], Meiyu Ke[a,b], Yong Cui[d], Zichen Chen[b], Chaofan Chen[a,b], Changyang Ji[d], Tuan Minh Tran[c], Liang Yang[c,e], Sin Man Lam[f], Yanhong Han[b], Guanghou Shui[f], Zhuang Wei[g], Shutang Tan[h], Kan Liao[g], Jiří Friml[i], Yansong Miao[c,j], Liwen Jiang[d,k], and Xu Chen[b,2]

[a]College of Life Science and Fujian Provincial Key Laboratory of Haixia Applied Plant Systems Biology, Fujian Agriculture and Forestry University, Fuzhou, Fujian 350002, China; [b]Fujian Agriculture and Forestry University–University of California, Riverside, Joint Center for Horticultural Biology and Metabolomics, Haixia Institute of Science and Technology, Fujian Agriculture and Forestry University, Fuzhou 350002, China; [c]School of Biological Sciences, Nanyang Technological University, 637551, Singapore; [d]School of Life Sciences, Centre for Cell and Developmental Biology and State Key Laboratory of Agrobiotechnology, The Chinese University of Hong Kong, 999077, Hong Kong; [e]Singapore Centre for Environmental Life Sciences Engineering, Nanyang Technological University, 637551 Singapore; [f]State Key Laboratory of Molecular Developmental Biology, Institute of Genetics and Developmental Biology, Chinese Academy of Sciences, Beijing 100101, China; [g]Key Laboratory of Systems Biology, CAS Center for Excellence in Molecular Cell Science, Shanghai Institute of Biochemistry and Cell Biology, Chinese Academy of Sciences, Shanghai 200031, China; [h]National Key Laboratory of Plant Molecular Genetics, CAS Center for Excellence in Molecular Plant Sciences, Shanghai Institute of Plant Physiology and Ecology, Chinese Academy of Sciences, Shanghai 200032, China; [i]Institute of Science and Technology Austria (IST Austria), 3400 Klosterneuburg, Austria; [j]School of Chemical and Biomedical Engineering, Nanyang Technological University, 637459, Singapore; and [k]The Chinese University of Hong Kong Shenzhen Research Institute, Shenzhen 518057, China

Plasmodesmata (PD) are plant-specific membrane-lined channels that create cytoplasmic and membrane continuities between adjacent cells, thereby facilitating cell–cell communication and virus movement. Plant cells have evolved diverse mechanisms to regulate PD plasticity in response to numerous environmental stimuli. In particular, during defense against plant pathogens, the defense hormone, salicylic acid (SA), plays a crucial role in the regulation of PD permeability in a callose-dependent manner. Here, we uncover a mechanism by which plants restrict the spreading of virus and PD cargoes using SA signaling by increasing lipid order and closure of PD. We showed that exogenous SA application triggered the compartmentalization of lipid raft nanodomains through a modulation of the lipid raft-regulatory protein, Remorin (REM). Genetic studies, superresolution imaging, and transmission electron microscopy observation together demonstrated that *Arabidopsis* REM1.2 and REM1.3 are crucial for plasma membrane nanodomain assembly to control PD aperture and functionality. In addition, we also found that a 14-3-3 epsilon protein modulates REM clustering and membrane nanodomain compartmentalization through its direct interaction with REM proteins. This study unveils a molecular mechanism by which the key plant defense hormone, SA, triggers membrane lipid nanodomain reorganization, thereby regulating PD closure to impede virus spreading.

Remorin | plasmodesmata closure | SA-controlled lipid order | membrane nanodomain compartmentalization

Plasmodesmata (PD) are highly plastic nanosized membrane-lined channels that serve as gatekeepers for cell-to-cell transportation and communication in plants (1). Previous ultrastructural analysis by transmission electron microscopy (TEM) have described PD as tunnels connecting neighboring cells, containing inner components of desmotubule, cytoplasmic sleeve, and deposited callose (2–4). Although these structural features of PD have been broadly described and the functions are essential, the mechanisms underlying PD permeability regulation are still poorly understood. Therefore, elucidating the regulatory mechanism of PD plasticity and its role in fine-tuning cell-to-cell communication are critical for understanding the functions of PD in plant development and responses to environmental stimuli.

The plant systemic acquired resistance (SAR) depends on the spreading of defense signals between cells and requires PD-mediated transportation (5). As channels connecting the symplastic cell-to-cell network, PD can also be hijacked by pathogens such as viruses to facilitate the trafficking of viral particles (6). On one hand, viruses spread from one cell to adjacent cells by manipulating the PD architecture (6). On the other hand, upon pathogen infection, plants induce SAR involving the local accumulation of

defense signals in the infected tissues (7, 8). One of the SAR-generated chemical signals, salicylic acid (SA), contributes to the regulation of PD permeability, and exogenous application of SA causes PD closure via regulation of callose deposition (9). Apparently, PD establish a battleground for plant defenses against pathogen attacks.

PD membranes are enriched in sterols and sphingolipids with very long chain saturated fatty acids (10), constituting crucial components of membrane lipid raft nanodomains (11, 12). Remorin (REM) represents one of the best-characterized membrane lipid nanodomain-localized proteins; its assembly pattern is critical for determining the formation of lipid nanodomains (13). In *Arabidopsis*, the REM family comprises 16 members (14). Individual REM proteins are associated with distinct membrane nanodomains, providing a platform for specific interactions between membrane lipids and membrane-resident proteins (15–17).

In this study, we adopted REM as a well-characterized nanodomain marker to investigate the correlation between membrane

Significance

Plasmodesmata (PD) create cytoplasmic and membrane continuities between adjacent cells to facilitate cell–cell communication and virus movement. Plant cells have evolved diverse mechanisms to regulate PD plasticity against plant pathogens, including the accumulation of the defense hormone, salicylic acid (SA). However, the mechanism of how this occurs is not well understood. Here, we uncover a mechanism by which SA triggers Remorin-dependent membrane lipid nanodomain assembly, leading to enhancement of the liquid-ordered phase. The higher-ordered lipids, which are particularly enriched at PD membrane, decreased PD membrane plasticity, and thus restricted PD opening and impeded virus spreading. Our findings address a knowledge gap in plant defense mechanisms at the membrane level that rely on SA-controlled lipid order and PD closure.

lipid raft compartmentalization and PD plasticity. We demonstrated that SA signaling has a direct impact on membrane nanodomain formation and PD closure. Based on the partition of membrane liquid-ordered/disordered phases, SA triggers recompartmentalization of lipid nanodomains and promotes ordered phase formation. PD membranes that are enriched with lipid components are greatly affected by SA, and PD permeability is attenuated by SA application. Remorin proteins serve as key regulators to coordinate the events of SA signaling, nanodomain organization, and PD structural plasticity. Altogether, our study underscores the fundamental role of SA in membrane lipid raft organization, uncovering the regulation of PD closure during defense responses.

Results

SA Causes PD Closure. To investigate the mechanism by which SA regulates PD permeability, we initially examined the ultrastructural changes of root meristematic cells in SA-treated wild-type (WT) plants. Using TEM, we observed that SA significantly impaired PD opening, as exhibited by long, narrow, and straight PD channels with 31- to 33-nm aperture, compared with the typical sandglass-shaped PD with a dilated neck and a 42- to 44-nm aperture in untreated plants (mock) (Fig. 1 A and B). PD density in the cell wall along the cell division plane (apical/basal sides) or along root growth axis (lateral sides) was not influenced by SA (Fig. 1C), indicating that PD structure is controlled locally by SA. To determine whether PD functionality is influenced by SA, we designed a dye-loading assay employing carboxy-fluorescein (CF) diacetate (CFDA) to track symplastic transportation (18, 19). CFDA assay showed that PD permeability was significantly blocked by SA (Fig. 1 D and E and Movies S1

and S2). Altogether, these data support the conclusion that SA caused PD closure and disrupted PD conductivity.

A previous study had demonstrated that SA-mediated PD closure relies on the deposited callose (9). We therefore tracked callose abundance by aniline blue staining and simultaneously used the PD-callose binding protein 1 (PDCB1), which binds callose (20), as another indicator to assay for callose location. SA significantly induced aniline blue-stained callose on both apical/basal and lateral cell sides (*SI Appendix*, Fig. S1 A and B). Similar to callose deposition, SA induced a PDCB1 signal on the lateral side, but PDCB1 signal was diminished on apical/basal sides (*SI Appendix*, Fig. S1 A–D). PDCB1 binds callose at PD and preferentially anchors to the sterol and sphingolipid-enriched membrane raft via glycosylphosphatidylinositol (GPI) motif (20–22). Therefore, the accumulation of PDCB1 to the lateral sides might be due to the overproduction of callose or to a rearrangement in the membrane system. To test these hypotheses, we used 2-deoxy-D-glucose (DDG), a callose synthesis inhibitor (23) (*SI Appendix*, Fig. S1 E and F), applied with SA-treated PDCB1-YFP (yellow fluorescent protein). DDG significantly disrupted the SA-induced PDCB1 signal on the lateral sides, whereas it did not fully inhibit the SA effect (*SI Appendix*, Fig. S1 A–D), indicating the existence of an additional, callose-independent mechanism of PD regulation downstream of SA signaling.

Lipid Rafts Are Essential for SA-Induced PD Closure. Compared with the surrounding plasma membrane (PM), PD membranes contain strikingly abundant lipid raft constituents that are homogeneously distributed and fundamental for PD functionality (10, 24, 25). We thus hypothesized that SA might influence PD aperture by modulating lipid rafts. Methyl-β-cyclodextrin (mβcd) is
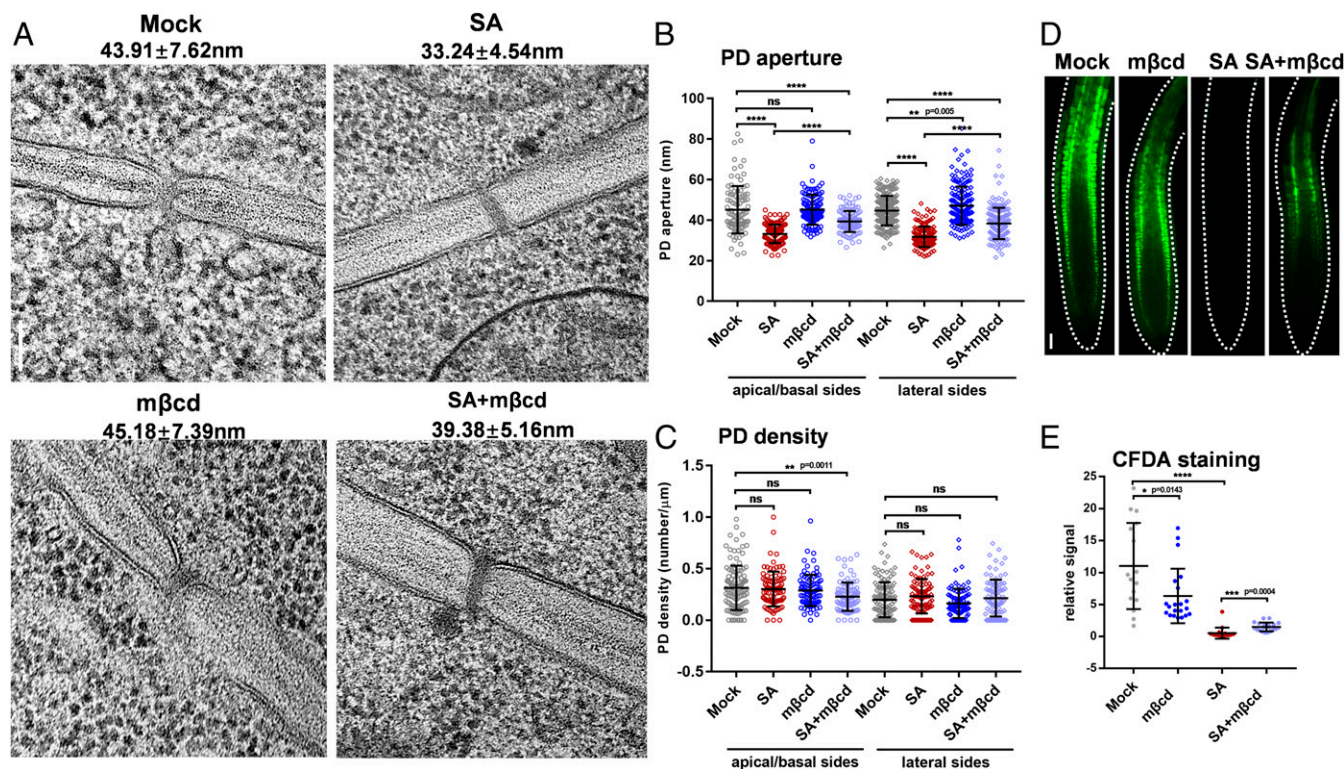

Fig. 1. SA causes PD closure. (A–C) PD structure was visualized by TEM, in root meristematic zone of mock, SA-treated (50 μM, 24 h), mβcd-treated (10 mM, 24 h), and SA-plus-mβcd–treated WT. PD aperture and density (number per micrometer) were observed and quantified on the apical/basal and lateral sides (B: n = 98, 134, 121, 112, 203, 145, 174, and 171; C: n = 115, 92, 92, 91, 115, 92, 92, and 91). (D and E) PD permeability was detected by CFDA assay in WT (100 μM SA, 10 mM mβcd, SA plus mβcd for 24 h), and PD permeability was quantified as CF signal in the root (E) (n = 16, 21, 19, and 20). (Scale bars: A, 100 nm; D, 10 μm.) Error bars represent SD. P values were determined by 2-tailed Student's t test (*P < 0.05, **P < 0.01, ****P < 0.0001; ns, not significant).

an efficient raft-disrupting agent and operates by depleting sterol from the membrane (11). To examine the possible relationship between SA and lipid raft on the control of PD aperture and conductivity, we treated WT with SA and mβcd separately or in combination. Although mβcd was not able to change callose level (*SI Appendix,* Fig. S1 *A* and *B*), mβcd and SA cotreatment efficiently impaired the SA effect on PD closure, as shown by a 39-nm PD aperture compared to a 33-nm PD after sole SA treatment (Fig. 1 *A* and *B*). PD density was not influenced by mβcd (Fig. 1*C*). This result showed that removal of sterols significantly offset the SA effect on PD closure, indicating that an appropriate order of the membrane lipid raft is essential for SA-mediated PD gating.

We next examined whether lipid rafts influence PD conductivity using CFDA assay. SA and mβcd cotreatment partially restored the inhibitory effect of SA on CF unloading (Fig. 1 *D* and *E*). Interestingly, mβcd also partially restored the SA effect on PDCB1 lateral accumulation (*SI Appendix,* Fig. S1 *C* and *D*). All of these data unequivocally support the notion that SA locally influences PD aperture and permeability through a lipid raft-dependent mechanism.

SA Increases the Proportion of Ordered Lipid Phase and Regulates the Compartmentalization of Membrane Nanodomains. We next investigated whether SA affects lipid raft organization in the PM.

Lipid rafts are defined as transient, relatively liquid-ordered membrane nanoscale domains (<200 nm), enriched in various sterols and sphingolipids (25). We stained WT roots using the widely used plant fluorescent probe, di-4-ANEPPDHQ, which is a styryl dye that senses the dipole potential changes of lipid bilayer (26). When di-4-ANEPPDHQ molecules detect the lipid domains with different dipole potential in the cell membrane, there is a large shift in the peak emission wavelength of the dye from 630 nm in liquid-disordered phase (nonnanodomain) to 570 nm in liquid-ordered phase (nanodomain) (26, 27) (*SI Appendix,* Fig. S2*A*). Compared with the nontreated plants, di-4-ANEPPDHQ displayed a significantly higher generalized polarization (GP) value (28) in SA-treated WT, suggesting that SA enhances the formation of an ordered membrane phase in the apical/basal or lateral PM (Fig. 2 *A* and *B* and *SI Appendix,* Fig. S2*B*). To validate this SA effect, we examined lipid order in the presence of mβcd, which depletes sterols, reducing the ordered phase. As expected, the GP value was significantly reduced by mβcd. Interestingly, mβcd also strongly attenuated the SA effect on shifting lipids toward the higher-ordered phase (Fig. 2 *A* and *B*). We then asked whether the pronounced effect of SA was dependent on SA signaling. Thus, we quantified the effect of SA-mediated lipid order in 2 mutants, the nonexpresser of PR gene 1
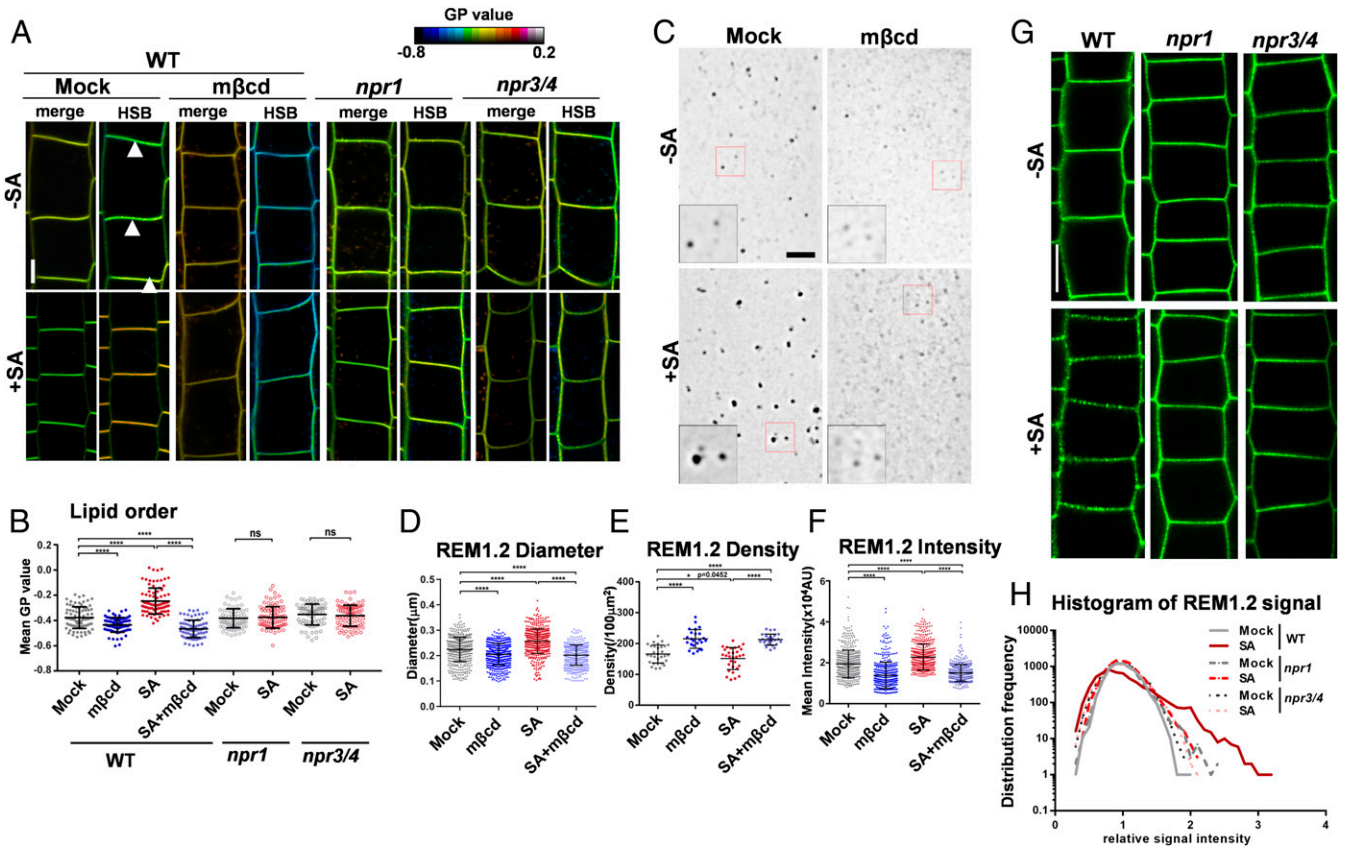

Fig. 2. SA triggers ordered lipid formation and induces REM assembly on the PM. (*A* and *B*) PM lipid order visualization in root meristematic cells. WT, *npr1,* and *npr3/4* seedlings were treated with mock (DMSO), SA (100 μM, 24 h), in the absence or presence of 10 mM mβcd (30 min), and then stained by di-4-ANEPPDHQ. The radiometric color-coded GP images were generated in HSB pictures. The white triangles indicate the membrane regions used for GP quantification (*A*) (*B*: n = 82, 78, 75, 73, 78, 85, 71, and 84). (*C*) *pREM1.2::GFP:REM1.2* seedlings were treated with SA (100 μM, 24 h), mβcd (10 mM, 30 min), or SA-plus-mβcd cotreatment, and GFP signal was observed by 2D-SIM. The *Inset* images display the 2× enlarged views of boxed areas in the original images. (*D–F*) Quantitative analysis of the individual GFP:REM1.2-marked nanodomains, with respect to diameter (*D*), density distribution (*E*), and intensity (*F*). n = 500 for each column in *D* and *F* from at least 10 images. The density graph (*E*) was generated by counting the nanodomain number in the selected regions of interest (n = 30, 24, 31, and 25). (*G* and *H*) REM1.2 distribution pattern was visualized by *pREM1.2::GFP: REM1.2* in *npr1* and *npr3 npr4* in the absence or presence of SA (100 μM, 24 h). (*H*) Chart represents the histogram of signal distribution frequency of REM1.2 signal (n = 6,282 [from 40 cells, 20 roots], 5,750 [38 cells, 16 roots], 6,437 [45 cells,13 roots], 8,205 [50 cells, 18 roots], 7,756 [51 cells, 16 roots], and 7,299 [43 cells, 16 roots]). (Scale bars: *A* and *G*, 5 μm; *C*, 2 μm.) Error bars represent SD. *P* values were determined by 2-tailed Student's *t* test (*P < 0.05; ****P < 0.0001; ns, not significant).

(*npr1*) and *npr3 npr4*, which are defective in SA perception (29, 30). Both *npr* mutants showed a strong resistance to lipid order upon SA stimulation (Fig. 2 *A* and *B*), indicating that the NPR receptor-mediated SA signaling regulates lipid order in the PM.

To provide insights into SA-dependent regulation on lipid raft organization at nanometer resolution, we employed super-resolution structured illumination microscopy (SR-SIM) to observe the lipid nanodomains using a well-studied nanodomain marker, REM. REM proteins are highly concentrated in sterol-enriched lipid environments and are required for the assembly of raft nanodomains (31). We constructed the green fluorescent protein (GFP) fused with coding sequences under the control of their native promoters plasmid and established stable transgenic *Arabidopsis* plants of *pREM1.2::GFP:REM1.2* and *pREM1.3::GFP:REM1.3*. Compared with a homogeneous distribution pattern of REMs in the PM of untreated plants, SA induced pronounced clusters of REM1.2 and REM1.3 proteins (*SI Appendix*, Fig. S2C). We then examined the GFP-REM1.2 signals by SR-SIM and used them as bona fide raft markers to quantitatively determine the compartmentalization of individual raft nanodomain. SA greatly enhanced the size of higher-signal intensity REM1.2-marked nanodomains but decreased nanodomain density (Fig. 2 *C*–*F*). The changes of nanodomain organization reported above are consistent with the overall increase in lipid order by SA. Owing to the importance of sterols for the ordered lipid phase formation (32), all SA-triggered changes in REM1.2-marked nanodomains were largely abolished by mßcd (Fig. 2 *C*–*F*).

We then tested the assembly pattern of REMs in *npr1* and *npr3 npr4* mutants by expressing *pREM::GFP:REM* in these mutants. In *npr1* and *npr3 npr4*, the SA impacts on REM1.2/1.3 clustering were largely abolished (Fig. 2 *G* and *H* and *SI Appendix*, Fig. S2 *D* and *E*). This provides evidence that NPR-dependent SA signaling organizes lipid raft nanodomains.

Arabidopsis inoculated with the plant pathogenic virus, cucumber mosaic virus (*CMV*), primes the induction of SA biosynthesis (33), which simulates the status of elevated SA level in vivo. To examine whether *CMV*-triggered endogenous SA accumulation causes a comparable assembly of REM-labeled nanodomains, we inoculated *pREM1.2::GFP:REM1.2* with *CMV*. As expected, *CMV*-infected roots also displayed obvious REM1.2 clusters, which were similar to the effects of exogenous SA application (*SI Appendix*, Fig. S2 *F*–*H*). Together, these data consistently showed that elevation of SA enhanced REM-labeled lipid raft nanodomain compartmentalization.

Remorins Are Crucial Regulators of Lipid Raft Formation and Plant Development. Lipid raft nanodomains are indispensable for controlling plant development, under physiological conditions as well as during pathogenic attack (34). Although recent biochemical studies have provided insights into the structural property of REM proteins and their potential functions in lipid raft organization (13, 16), the genetic analysis of REM has remained limited owing to the functional redundancy of these proteins. To examine the expression profiles of 16 *Arabidopsis* REM homologs (15), we performed qRT-PCR to search for root-abundant REMs. Our results showed that the *REM1* subfamily, especially *REM1.2*, *REM1.3*, and *REM1.4* were ubiquitously expressed in most tissues (*SI Appendix*, Fig. S3 *A*–*E*). Of all REMs, the sequences of REM1.2 and REM1.3 were mostly closely matched (14), and therefore most likely to be redundant. We also identified null alleles of *rem1.2* and *rem1.3* single mutants (*SI Appendix*, Fig. S3 *F*–*H*), and neither of them displayed significant developmental defects. We then generated 2 independent *rem1.2 1.3* double mutants by designing a CRISPR-Cas9–mediated REM1.3 knockout in *rem1.2* mutant, termed *rem1.2 1.3c*. We validated the mutation of REM1.2 and REM1.3 knockouts by Western blotting (*SI Appendix*, Fig. S3 *I* and *J*). Further phenotypic analysis revealed that *rem1.2 1.3c* mutants

exhibited much smaller cotyledons than WT and single mutants (Fig. 3 *A* and *B*).

We also generated plant lines that conditionally overexpressed REM1.2 and REM1.3 lines using the β-estradiol–inducible system (XVE) (35), termed *XVE:REM* lines. We obtained several independent *XVE:REM1.2* and *XVE:REM1.3* lines (*SI Appendix*, Fig. S3 *K* and *L*), and all of them consistently displayed severely dwarf plants, short and agravitropic roots when continuously growing on estradiol-supplemented medium (Fig. 3 *C* and *D*, *SI Appendix*, Fig. S3O, and Movies S3 and S4). Validation by Western blotting showed that the quantity of REM proteins was gradually elevated in a time course manner of estradiol induction and reached maximal levels at 24 h postinduction (*SI Appendix*, Fig. S3 *M* and *N*).

To further access the role of REM1.2/1.3 in lipid raft formation, we stained roots of overexpressed REM1.2 line and *rem1.2 1.3c* by di-4-ANEPPDHQ to examine the lateral segregation of lipid species into liquid-ordered or liquid-disordered phases. The transient and robust induction of REM1.2 (*XVE:REM1.2*) generated significantly higher GP values, indicating an increased level of ordered lipid domains on the PM (Fig. 3 *E* and *F*). A coincubation with mßcd entirely abolished the lipid order change in *XVE:REM1.2* (Fig. 3 *E* and *F*). The *rem1.2 1.3c* mutant did not show obvious changes on lipid order (Fig. 3 *G* and *H*). We then examined the sensitivity of *rem1.2 1.3c* mutant to SA-triggered higher ordered lipid formation using a serial concentration of SA. We observed a clear difference in lipid order between *rem1.2 1.3c* and WT under the treatments using 25 and 50 μM SA, respectively. Thus, *rem1.2 1.3c* showed significantly less sensitivity to lipid order change upon SA elicitation compared with WT (Fig. 3 *G* and *H*).

We next asked whether the increase in lipid order and nanodomain compartmentalization by SA or REM overproduction is due to REM clustering or the change of lipid species. We performed a lipidomics analysis to compare lipid components upon SA treatment or in REM mutants and overexpressed plants. We did not observe strong lipid imbalance in SA-treated WT, *rem1.2 rem1.3c* mutant, or *XVE:REM1.2* line, except for slight changes in several phosphatidylinositol, phosphatidylglycerol, phosphatidylcholine, phosphatidic acid, and phosphatidylserine species (*SI Appendix*, Fig. S4 and Datasets S1–S3). It is worthy to note that neither SA treatment nor REM transgenic plants were able to change the levels of sphingolipids and sterols, which are the typical nanodomain lipid components (*SI Appendix*, Fig. S4 *A* and *B* and Datasets S1 and S2). Taken together, these data indicate that, without significantly changing the abundance of sterol and sphingolipid components, a modulation of REMs clustering is sufficient to regulate lipid order on the PM as well as the compartmentalization of raft nanodomains. The lipidomics data suggest a primary role of REM clustering in fine-tuning SA-mediated nanodomain assembly.

Remorins Regulate Plasmodesmal Aperture and Functionality. Previous studies have shown that particular lipid components are enriched in PD membranes rather than in the surrounding PM (10), suggesting that SA regulates lipid order to change PD functionality. To examine PD functionality, we first detected PD permeability in *rem* mutants and overexpressors by CFDA assay. CF signals in the root tip showed that PD permeability was enhanced in *rem* mutants, whereas it declined in REM overexpressors (*SI Appendix*, Fig. S5 *A*–*C*). Moreover, using a functional complementation test by introducing *pREM::GFP:REM* in *rem1.2* or *rem1.3*, respectively (called *rem1.2-Comp* or *rem1.3-Comp*), we showed that PD permeability in the complementation lines was restored to almost a WT level (*SI Appendix*, Fig. S5 *A* and *C*), confirming that REMs are key components involved in PD-mediated symplastic communication.
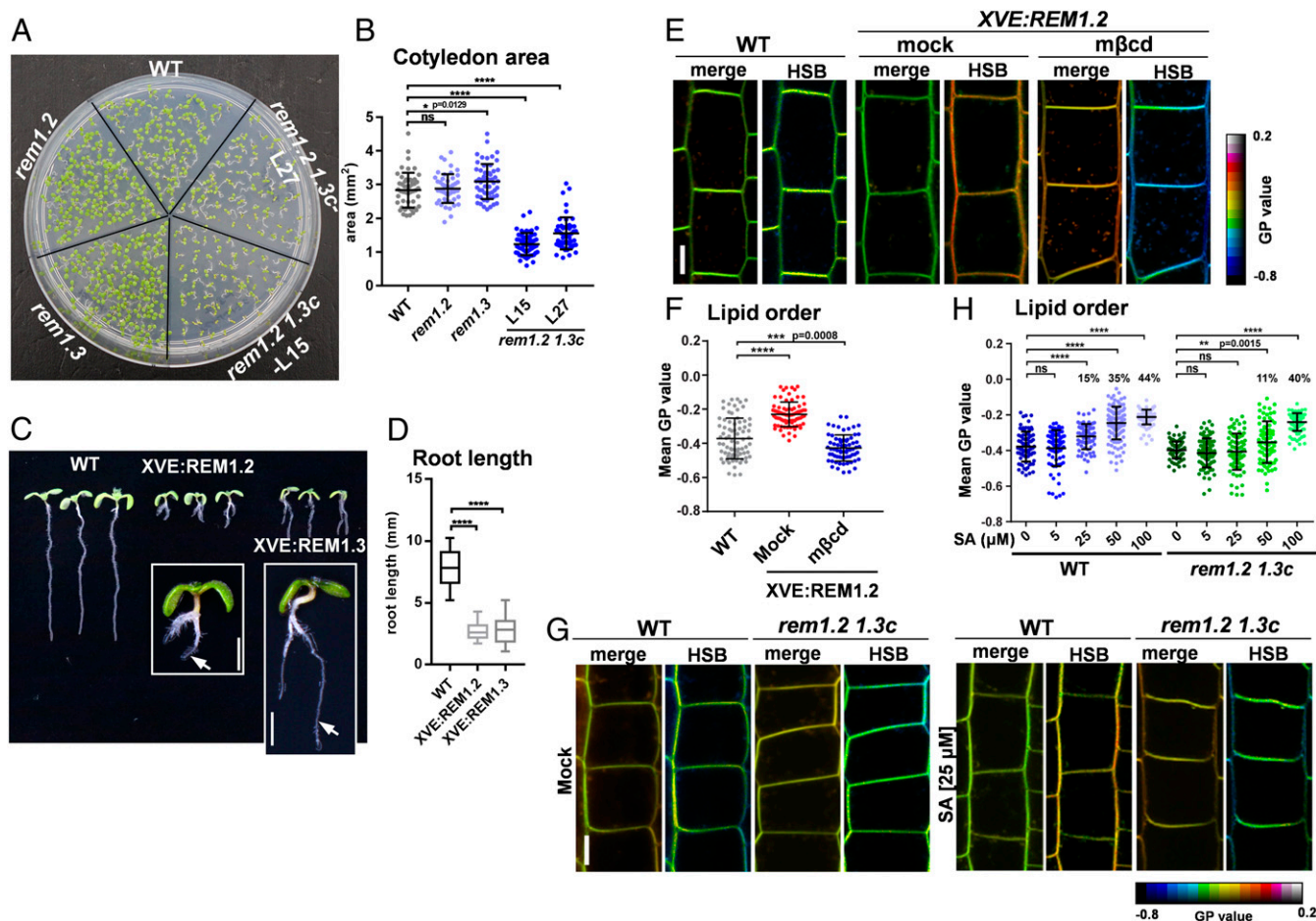
Fig. 3. Remorins are crucial regulators for proper lipid order formation. (*A* and *B*) Phenotypes of 5-d-old *rem1.2*, *rem1.3* single mutants, and 2 independent *rem1.2 1.3c* double mutants (L15 and L27). Cotyledon areas were quantified (*B*: n = 50, 50, 54, 55, and 52). (*C* and *D*) WT, *XVE:REM1.2*, and *XVE:REM1.3* were germinated and continuously grown on 5 μM estradiol-supplemented medium for 8 d. Enlarged pictures of *XVE:REM1.2* and *XVE:REM1.3* are shown in the *Inset* boxes, and the arrows highlight the primary roots (*C*). Primary root length was quantified (*D*: n = 40, 40, and 42). (*E* and *F*) Lipid order visualization in root cells of WT and *XVE:REM1.2* (±10 mM mβcd, 30 min), which were stained by di-4-ANEPPDHQ. GP value was quantified (*F*: n = 76, 77, and 67). (*G* and *H*) Lipid order was tested in WT and *rem1.21.3c*, which were treated with a serial concentration of SA for 24 h, followed by di-4-ANEPPDHQ staining. GP value was quantified (*H*: n = 80, 78, 73, 118, 93, 88, 85, 78, 74, and 102). The percentages indicate the increase ratios of GP value induced by SA treatments comparing with each mock treatment. (Scale bars: *C*, 2 mm; *E* and *G*, 5 μm.) Error bars represent SD. *P* values were determined by 2-tailed Student's *t* test (*P < 0.05, **P < 0.01, ***P < 0.001, ****P < 0.0001; ns, not significant).

To clarify the regulatory mechanism by which REM regulates PD permeability, we examined the subcellular distributions of REM1.2 and REM1.3 by immunogold labeling on *pREM::GFP:REM* seedlings. Compared with the negative control of the antibody added to WT cells or no antibody in *pREM1.3::GFP:REM1.3* cells (*SI Appendix*, Fig. S6*A*), gold particles against GFP in GFP:REM cells showed a clear localization of REM1.2 and REM1.3 in the PM as well as at PD, supporting the functionality of REMs at PD and PM (Fig. 4*A*).

We next analyzed the ultrastructural structure of PD in *rem* mutants and overexpressors by TEM. Since there is a differential expression pattern of REM1.2 and REM1.3 in the cortex and endodermis of root cell layers (*SI Appendix*, Fig. S5*A*), we analyzed the PD structure of *rem* mutants in cortex and endodermis, respectively. Although the canonical architecture of PD was intact, PD aperture was significantly modified in *rem* mutants and overexpressors. On the apical/basal sides of WT cells, we saw a ~40-nm aperture of PD channels, compared with a wider ~43-nm PD aperture in *rem1.2* and *rem1.3* mutants. Moreover, *rem1.2 1.3c* had an even wider PD aperture of ~48 nm (Fig. 4 *B* and *C*). In contrast, *XVE:REM1.2* and *XVE:REM1.3* exhibited severely impaired PD openings and exhibited narrow PD channels (~36 nm), similar to

SA-treated WT plants (Figs. 1 *A* and *B* and 4 *B* and *C*). Consistent with the PD phenotypes on apical/basal sides, *rem* mutants promoted and *XVE:REM1.2* impaired PD opening also on the lateral sides (*SI Appendix*, Fig. S6*B*). Thus, REM proteins function as negative regulators involved in the modulation of PD gating. Similar to the effects of SA, *rem* mutant and overexpressors were not able to alter PD density (*SI Appendix*, Fig. S6*C*), further supporting a specific role for REM in control of PD aperture.

To examine PD structure in-depth, we reconstructed ultrastructural PD morphology by 3D electronic tomography. Representative 3D-PD structures of *rem* mutants and overexpressors revealed that *rem1.2* and *rem1.2 1.3c* mutants had wider PD aperture and apparent cytoplasmic sleeves between the desmotubule and the PM, whereas cytoplasmic sleeves disappeared in *XVE:REM1.2* (Fig. 4*B*, *SI Appendix*, Fig. S5*D*, and Movies S5–S8). Thus, 2D and 3D TEM observations unequivocally demonstrated that REMs are crucial regulators for determining the diameter of PD channels. We then used *pSUC2-GFP* as an additional indicator of PD conductivity (36). CFDA assay or expressing *pSUC2-GFP* in *XVE:REMs* both showed that PD
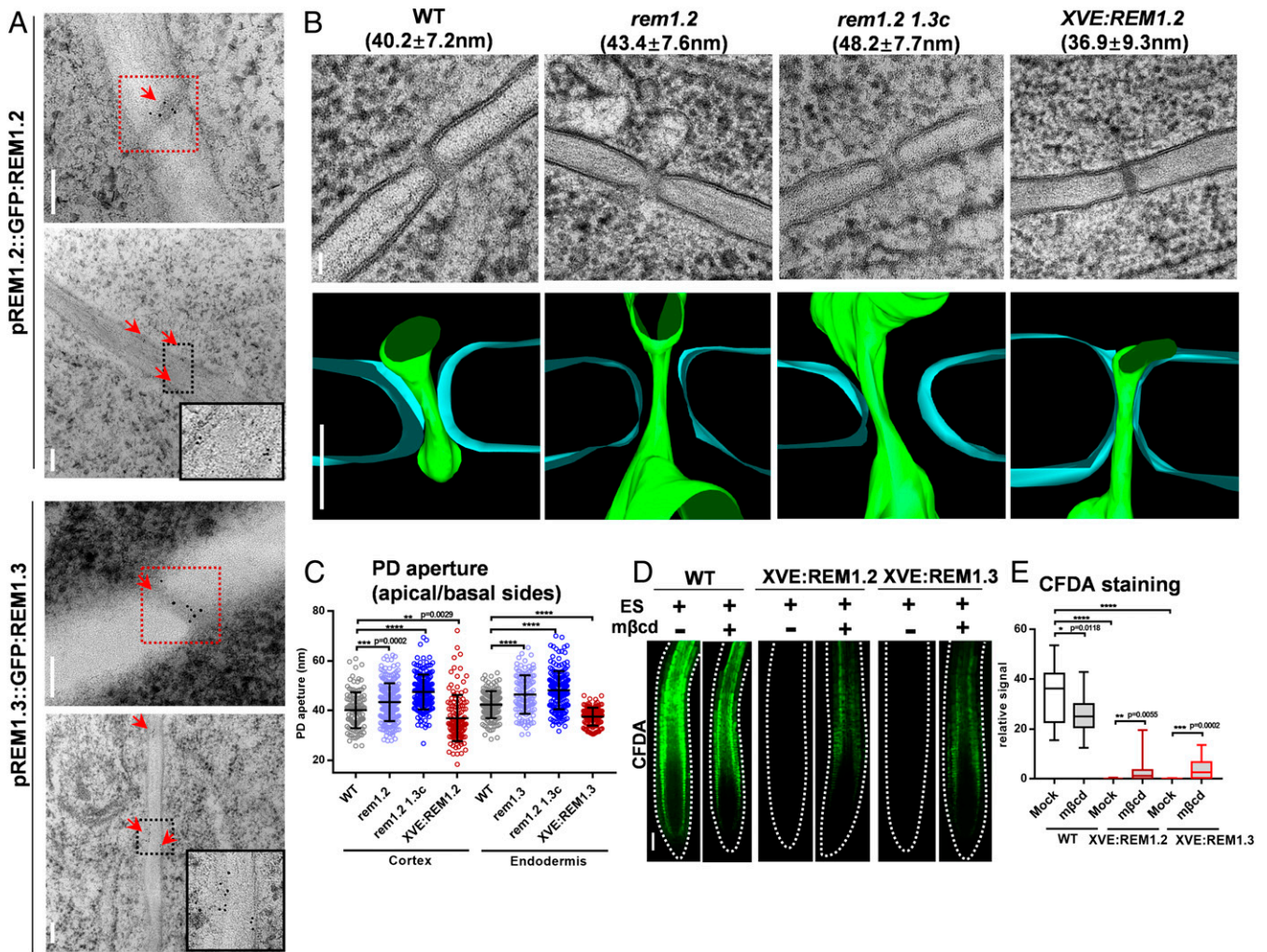
Fig. 4. *Rem* mutants increase and overexpressed REMs decrease PD aperture. (*A*) REM1.2 and REM1.3 proteins were detectable at PM and PD by immunogold labeling with GFP antibody. The red boxes indicate PD and the black boxes indicate PM, and the arrows highlight the gold-labeled REMs. The *Inset* images display the 2× enlarged views of boxed areas in the original images. (*B* and *C*) PD structure was visualized by TEM in WT, *rem* mutants, and *XVE:REM* at the cell layers of cortex and endodermis, respectively. PD aperture was quantified on the apical/basal sides (*C*: n = 120, 228, 179, 126, 150, 125, 182, and 126). Tomographic slices and 3D models show dimensional PD structures. ER (green) structure and PM (blue) are differently color-coded (*B*, *Lower*). (*D* and *E*) WT and *XVE:REM1.2/1.3* seedlings were treated with 10 mM mβcd for 24 h, compared with nontreated samples. PD permeability was measured by CFDA assay (*E*: n = 19, 20, 22, 17, 20, and 19). (Scale bars: *A* and *B*, 100 nm; *D*, 10 μm.) Error bars represent SD. *P* values were determined by 2-tailed Student's *t* test (*P < 0.05, **P < 0.01, ***P < 0.001, and ****P < 0.0001).

conductivity was severely blocked in *XVE:REMs* (Fig. 4 *D* and *E* and *SI Appendix*, Fig. S6 *D–F*).

We next asked whether such REM-mediated PD closure requires key nanodomain components, such as the plant phytosterols. To test this, mβcd, which depletes membrane sterols, was applied to *XVE:REMs*. mβcd significantly restored the weak unloading of CFDA or aberrant expression of the GFP signal in *XVE:REM* lines (Fig. 4 *D* and *E* and *SI Appendix*, Fig. S6 *E* and *F*), further supporting the importance of lipid raft in REM-mediated PD closure. To further examine whether REM-stimulated callose overproduction resulted in PD closure (37), we also applied DDG in *XVE:REM1.2 SUC2-GFP*. The decreased callose level as a result of DDG treatment was not able to rescue the impaired SUC2-GFP signal in *XVE:REM1.2* line (*SI Appendix*, Fig. S6 *E* and *G*). Therefore, we conclude that REM-dependent lipid raft organization is necessary to maintain appropriate PD aperture and permeability.

Remorins-Mediated PD Closure Is Downstream of SA Signaling. The discovered SA effect on the assembly of REM1.2/1.3 proteins and the compartmentalization of membrane nanodomains

motivated us to test whether REM would also functionally regulate lipid rafts downstream of SA-mediated signaling pathways. Transcript abundance of *REM*s was slightly elevated by SA; meanwhile, protein levels of REM1.2 and REM1.3 were also elevated 1.4- to 1.7-fold upon SA stimulation (Fig. 5*A* and *SI Appendix*, Fig. S7 *A* and *B*).

To prove the functionality of REMs in SA-mediated PD closure, we examined the sensitivity of *rem1.2 1.3c* mutant to SA using CFDA assay. CFDA-indicated PD permeability of SA-treated WT was decreased to 5% upon 100 μM SA treatment, compared with nontreated WT (Fig. 5 *B* and *C* and *SI Appendix*, Fig. S7 *C* and *D*). In contrast, SA was less effective in *rem1.2 1.3c* double mutant, compared with WT (Fig. 5 *B* and *C* and *SI Appendix*, Fig. S7 *C* and *D*). To further dissect the functional correlation between REMs and the SA signaling receptors NPRs, we overexpressed REM1.2 and REM1.3 in *npr1* and *npr3 npr4* mutants. Compared with the background plants from which the *XVE:REMs* or *npr* mutants were derived, the leaf and root morphology of *XVE:REMs npr1* and *XVE:REMs npr3 npr4* all
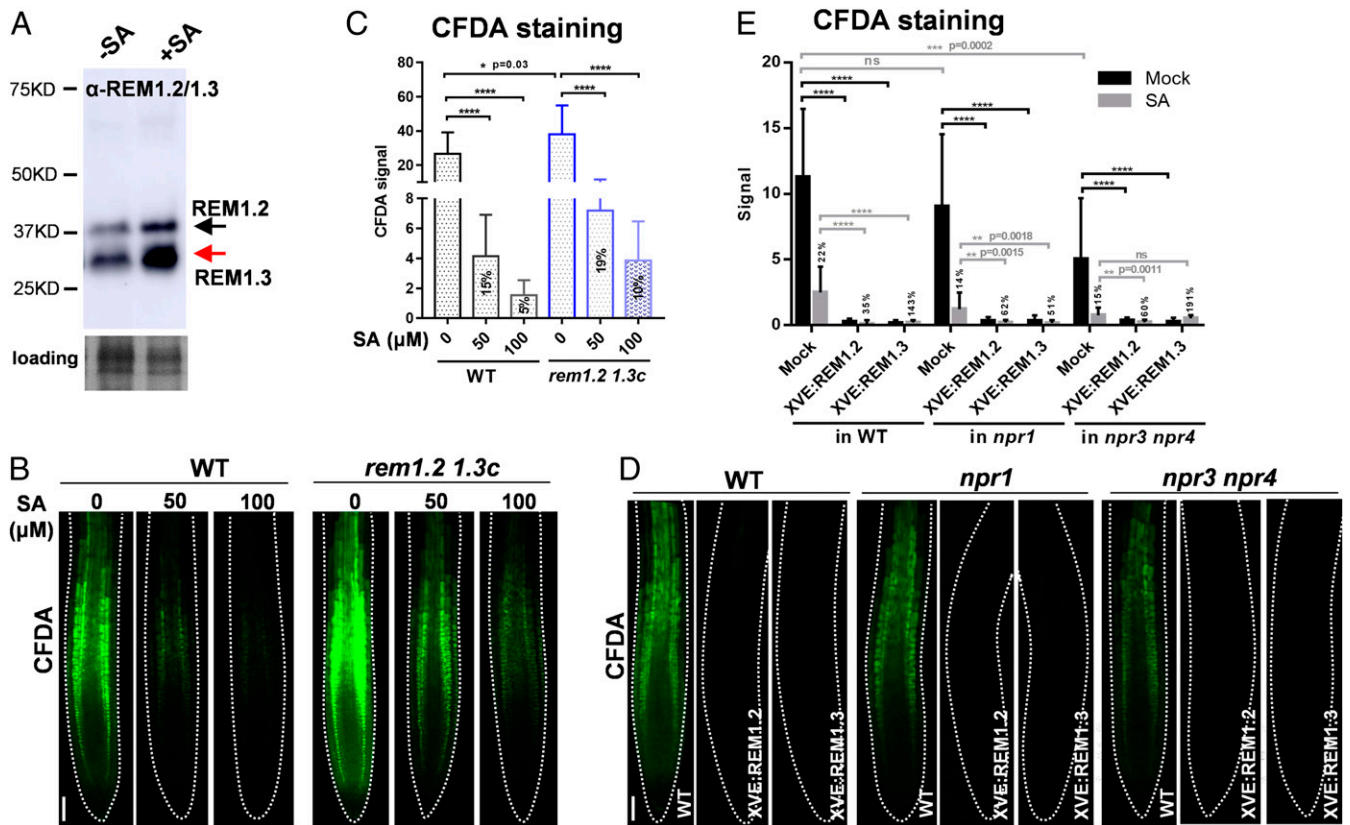
Fig. 5. REMs are crucial regulators involved in SA signaling pathway. (*A*) Protein level of REM1.2 and REM1.3 (labeled as arrows) was detected in WT seedlings by Western blotting (with REM1.2/1.3 antibody) with or without SA treatment (100 μM, 24 h). (*B–E*) PD permeability was detected by CFDA assay. The 50 or 100 μM SA was applied for 24 h in WT and *rem1.2 1.3c* (*n* = 17, 16, 16, 17, 16, and 16) (*B* and *C*). *rem* mutants, *npr* mutants, and *XVE:REM npr* seedlings were treated with or without SA (50 μM, 24 h) treatment (*n* = 22, 18, 19, 19, 18, 20, 22, 17, 18, 18, 18, 18, 19, 18, 19, 18, 18, and 18) (*D* and *E*). The percentage indicates the signal ratio to compare SA-treated group with each mock, respectively. (Scale bars: *B* and *D*, 10 μm.) Error bars represent SD. *P* values were determined by 2-tailed Student's *t* test (**P < 0.01, ***P < 0.001, ****P < 0.0001; ns, not significant).

resembled *XVE:REMs* (*SI Appendix*, Fig. S7*E*). CFDA assay in the above lines consistently showed that PD permeability in *XVE:REMs npr1* and *XVE:REMs npr3 npr4* was severely compromised, similar to *XVE:REMs* (Fig. 5 *D* and *E*). Thus, REMs are epistatic to NPRs involved in SA signaling.

14-3-3 Protein Acts as an Adaptor to Maintain the Assembly Pattern of REM and Membrane Nanodomains. To address how SA regulates REM proteins and lipid raft assembly, we used *pRE-M1.2::GFP:REM1.2* stable transgenic seedlings to screen for candidate proteins interacting with REM1.2 by immunoprecipitation coupled to mass spectrometry (IP-MS) assay. Analysis of IP-MS data revealed that several isoforms of 14-3-3 protein, including 14-3-3 epsilon (general regulatory factor 10 [GRF10]), chi (GRF1), mu (GRF9), omega (GRF2), nu (GRF7), and phi (GRF4) were obtained among proteins that coimmunoprecipitated (co-IP) with REM1.2 (Dataset S4). We further performed co-IP to confirm these protein–protein interactions in vivo using overexpressed GFP-tagged REM1.2 transgenic *Arabidopsis* plants (GFP-REM1.2). Interestingly, when REM1.2 proteins were pulled down by GFP magnetic beads, the proteins at the molecular weight of 14-3-3 monomers and dimers were both detectable in GFP-REM1.2 line, compared with only the monomer 14-3-3 bands in WT (Fig. 6*A*), implying that 14-3-3 might work together with REM through its dimeric form.

In an attempt to examine whether REMs and 14-3-3 interaction exists under in vivo physiological condition in plant, we applied the bimolecular fluorescence complementation (BiFC)-luciferase (Luc) reconstitute imaging assay (38) by coexpressing

GRF-nLUC and cLUC-REM in Nicotiana *benthamiana* leaves (*SI Appendix*, Fig. S8*A*). When sprayed with luciferin to detect maximum Luc-complementation activity for both REM1.2-GRFs and REM1.3-GRFs, only pairs of REM1.2-GRF10 and REM1.3-GRF10 showed a strong reconstituted Luc-signal, compared with the negative controls (*SI Appendix*, Fig. S8 *B* and *C*). These results demonstrated that REM1.2 and REM1.3 interact with GRF10 protein in plants. We then performed a yeast 2-hybrid assay to test the existence of a physical interaction between REM1.2/1.3 and GRF10. Compared with the negative controls, the positive colonies of GRF10-REM1.2/1.3 pairs on the selective yeast medium (SD/-LTHA) confirmed that GRF10 directly interacted with REM proteins (*SI Appendix*, Fig. S8*D*).

The 14-3-3 protein has a wide range of roles in cell signaling pathways within the nucleus, cytoplasm, and PM (39–43). To understand the location for REM1.2/1.3 and GRF10 interaction, we utilized the BiFC-YFP system to coexpress GRF-n/cYFP and n/cYFP-REM in *N. benthamiana* leaves. Compared with the negative controls, GRF10-REM pairs showed strong reconstituted YFP signal on the PM, which was colocalized with FM4-64–labeled membrane (Fig. 6*B* and *SI Appendix*, Fig. S8 *E* and *F*), indicating that GRF10 directly binds to REM proteins on the PM. Interestingly, detection of GRF10 protein level by separately extracting total proteins or membrane-associated proteins showed that SA significantly enhanced membrane-associated of GRF10, whereas the total protein abundance of GRF10 was not changed (Fig. 6*C*). These data imply that GRF10 might act as a stabilization factor to mediate the oligomerization of REM on the PM.
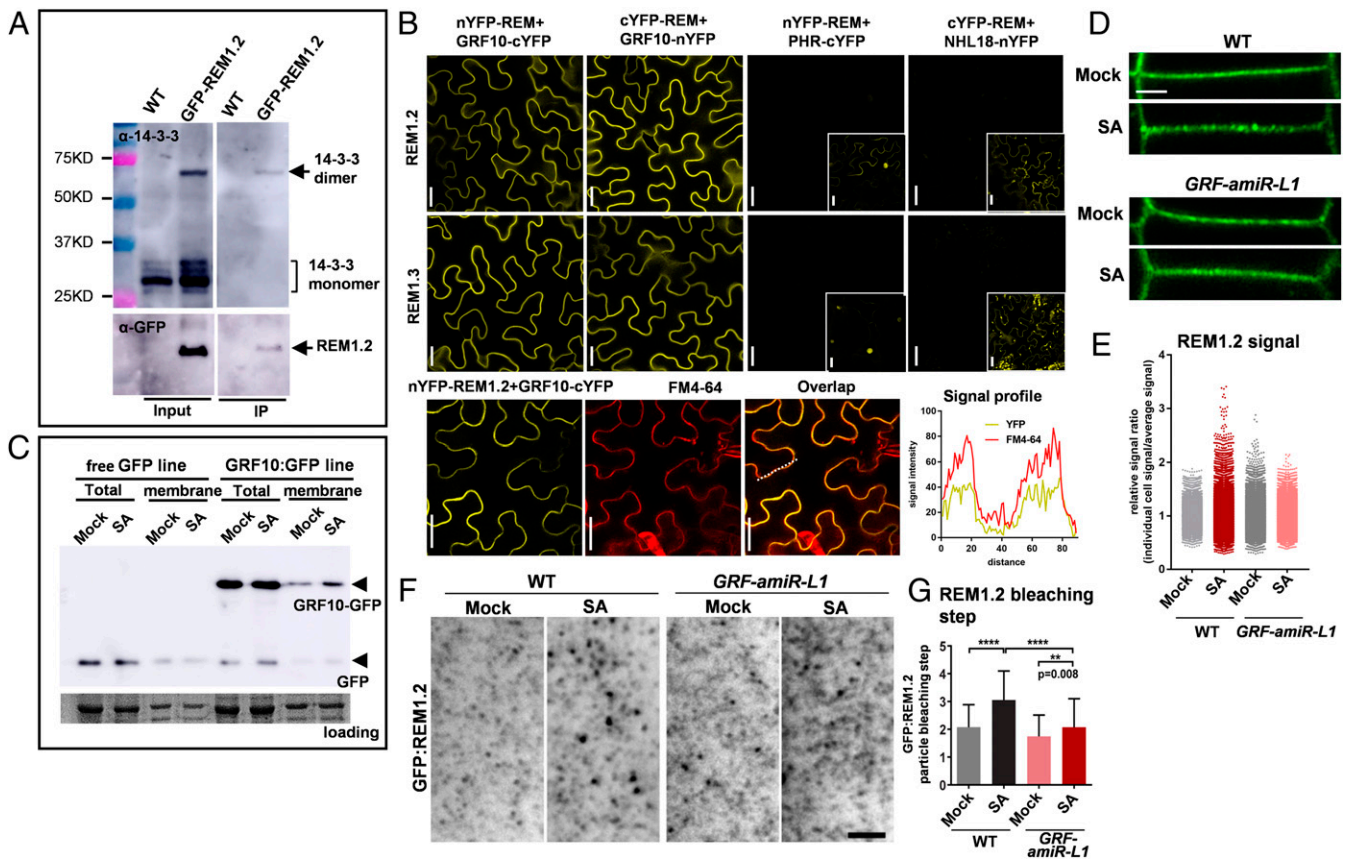
Fig. 6. 14-3-3 proteins interact with REMs and are required for REM oligomerization and assembly. (*A*) Co-IP showed the interaction between REM1.2 and 14-3-3. GFP-tagged REM1.2 were immunoprecipitated by GFP magnetic beads. The coimmunoprecipitated 14-3-3 proteins were detected by the endogenous 14-3-3 antibody. Monomeric and oligomeric 14-3-3 proteins are marked according to molecular weight. The corresponding blot detected by the GFP antibody was used as the positive control. Input indicates the flow-through samples before the incubation of GFP beads. (*B*) BiFc-YFP system shows the interactions of REMs with GRF10. REMs and GRFs were individually fused with nYFP or cYFP. BiFc pairs of other unrelated n/cYFP with n/cYFP-REM are shown as negative controls. The pictures with increased laser setting of weak signal are shown in the *Bottom Right* corner. *Lower* panels show the colocalization between FM4-64–labeled PM (red) and REM1.2–GRF10 interaction (yellow). Colocalization signal profile chart was generated based on the white dot line. (*C*) Total protein and membrane protein levels of GRF10 were detected in *35S:GFP* or *35S::GRF10:GFP* seedlings by Western blotting (with GFP antibody) under mock or SA treatment (100 μM, 24 h). GRF10-GFP and GFP proteins are individually labeled as arrows according to molecular weight. (*D* and *E*) *pREM1.2::GFP:REM1.2* signal was visualized in WT or *GRF-amiR-L1* background (with estradiol induction) with mock or SA (100 μM, 24 h) (*D*). (*E*) Chart represents the relative signal profile of REM1.2 signal intensity in different genotypes along the PM upon mock or SA treatment (n = 11,642 [from 58 cells, 18 roots], 8,315 [42 cells, 15 roots], 11,522 [51 cells, 17 roots], and 11,814 [55 cells, 13 roots]). (*F* and *G*) VAEM image of *pREM1.2::GFP:REM1.2* in WT or *GRF-amiR-L1* roots by mock and SA (100 μM) treatment for 24 h (*F*). Stepwise photobleaching counting experiments of GFP:REM1.2 (n = 105, 100, 111, and 125) in *G*. (Scale bars: *B*, 50 μm; *D*, 2 μm; and *F*, 1 μm.) Error bars represent SD. *P* values were determined by 2-tailed Student's *t* test (**P < 0.01, ****P < 0.0001).

Increasing evidence has shown that 14-3-3 serves as primary pathogen targets in plant immunity (44, 45), and a 14-3-3 protein was significantly enriched in detergent-resistant membranes upon cryptogein treatment (46). To examine the contribution of GRF10 in mediating REM oligomerization, we firstly generated a GRF10-deficient mutant to silence the 14-3-3 epsilon subfamily, GRF9 and GRF10 simultaneously (called *GRF-amiR* lines). These lines displayed growth defects with a higher incidence of root agravitropism (*SI Appendix*, Fig. S9 *A* and *B*), consistent with the prior publication (47). Furthermore, we introduced *pREM1.2::GFP:REM1.2* into *GRF-amiR-L1* to investigate the assembly pattern of REM1.2 proteins on the PM. Strikingly, GFP:REM1.2 assemblies were no longer enhanced by SA in *GRF-amiR-L1* seedlings, compared with SA effects on GFP-REM1.2 in WT (Fig. 6 *D* and *E* and *SI Appendix*, Fig. S8 *G* and *H*). Using the variable-angle epifluorescence microscopy (VAEM) approach in *GRF-amiR-L1*, the brighter punctuates of GFP-REM1.2 that were previously induced by SA in WT plants were no longer clustered on PM upon SA treatment (Fig. 6*F*). A fluorescent bleaching assay demonstrated that SA directly

induced the formation of the higher-order protein oligomerization of GFP-REM1.2; however, this oligomerization disappeared in *GRF-amiR-L1* (Fig. 6*G* and *SI Appendix*, Fig. S8*I*), suggesting a GRF10-mediated REM clustering and protein oligomerization on the PM under SA exposure. Correspondingly, PD permeability analysis by CFDA assay showed that *GRF-amiR-L1* was insensitive to the SA effect on PD closure (*SI Appendix*, Fig. S9*D*). Therefore, we conclude that 14-3-3 protein acts as an adaptor to maintain the organizational pattern of REM and membrane nanodomains.

Remorins Are Important Regulatory Components of Plant Defense to Virus. Through the dynamic control of PD aperture by SA signaling, plants may establish an unelucidated defense system against virus infection. In order to verify this hypothesis, we inoculated *N. benthamiana* leaves with agrobacterial strains that harbored 35S:RFP-REM1.2/1.3 or 35S:RFP (control), together with a modified tobacco rattle virus (*TRV*)-GFP (48) to assess the impact of the altered cell-to-cell movement of virus. We used fluorescent microscopy to analyze the size of *TRV* infection foci
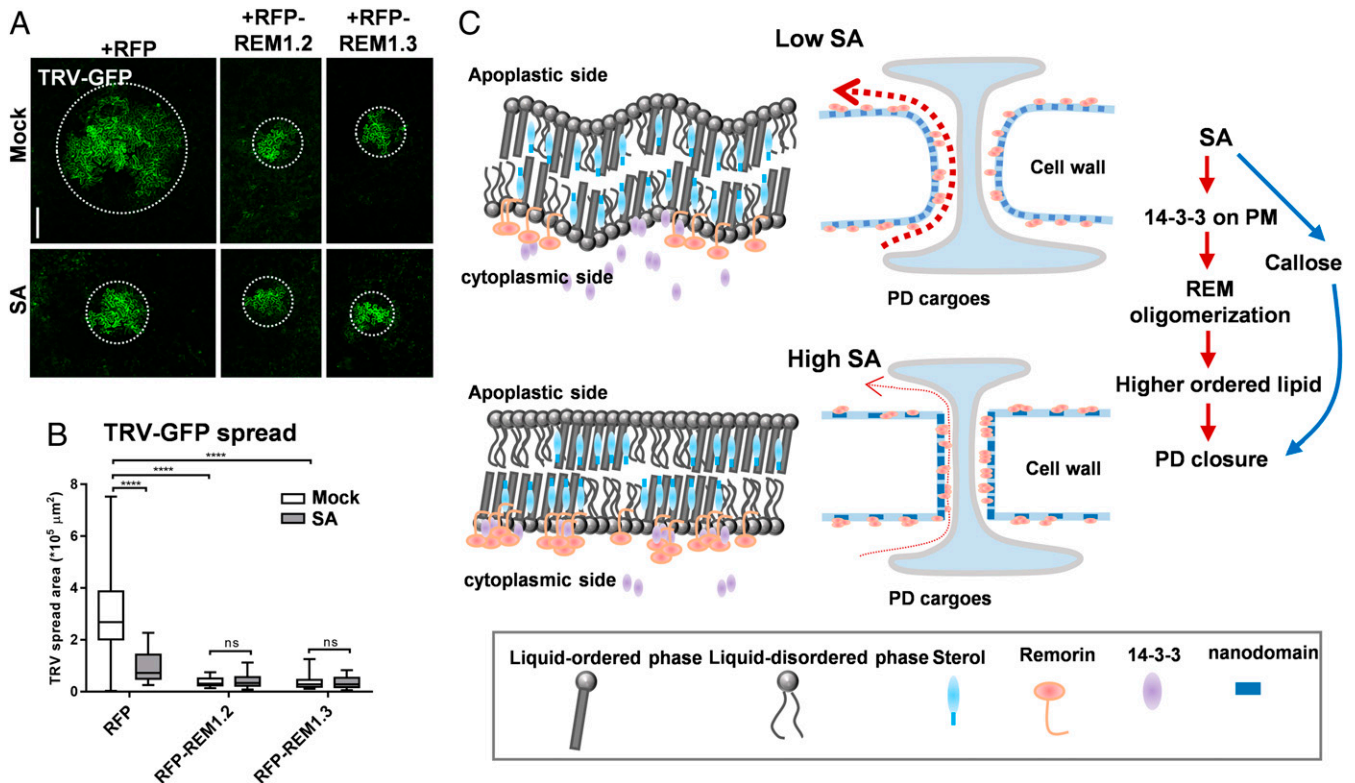
Fig. 7. Model of SA-mediated plant defense response by REM-dependent lipid raft organization. (*A* and *B*) TRV–GFP. *N. benthamiana* leaves were coinfiltrated with agrobacterial strains containing diluted TRV1 and TRV-GFP as well as 35S:RFP-REM1.2/1.3. Infection efficiency of TRV-GFP was quantified. Coinfiltration of TRV/TRV1-GFP and 35S:RFP was used as a control. The 100 μM SA was sprayed, and GFP spread areas were observed and quantified at 5 dpi (n = 33, 32, 35, 35, 30, and 31). (*C*) Speculated models: Membrane system shows tighter packed liquid-ordered phase (nanodomain) and less packed liquid-disordered phase (nonnanodomain). The ordered lipid phase requires the integration of sterols. Under low-SA conditions, the ordered and disordered phases of lipids are homogeneously distributed and well organized by monomer/oligomer states of REM proteins, maintaining PD membrane plasticity. Under high-SA conditions, REM oligomers are recruited by 14-3-3 dimers on the PM; REM clusters cause nanodomain compartmentalization and higher-ordered lipid phase, thereby reducing membrane plasticity to block PD opening. The red arrows with dotted lines represent the possible efficiency of PD cargoes movement during low- or high-SA circumstance. The *Right* panel shows the possible signaling transduction described in this study. (Scale bars: *A*, 200 μm.) Error bars represent SD. P values were determined by 2-tailed Student's t test (****P < 0.0001; ns, not significant).

at 5 d after inoculation to reveal the efficiency of virus particle movement. In RFP-inoculated leaves, exogenous SA significantly decreased *TRV-GFP* spreading area to one-third of that of the nontreated sample (Fig. 7 *A* and *B* and *SI Appendix*, Fig. S10). In contrast, overexpressed RFP-REMs pronouncedly restricted *TRV-GFP* movement, in line with our conclusion that overexpressed REMs conferred PD closure (Fig. 7 *A* and *B* and *SI Appendix*, Fig. S10). Collectively, these results provide robust evidence for the involvement of REM-dependent lipid raft organization in SA-triggered plant defense pathway.

Discussion

Accumulating evidence indicates that membrane lipid rafts act as platforms to mediate spatiotemporal organization of protein complexes, thereby influencing downstream cellular cascades (49–51). In particular, during pathogen infection, membrane lipid rafts are essential to establish the appropriate pathogen recognition sites, providing a large surface area for pathogen colonization. In our study, we have revealed that high SA promotes the assembly of lipid nanodomains, leading to the enhancement of the liquid-ordered phase. The higher-ordered lipids, which are particularly enriched at the PD membrane, might decrease PD membrane plasticity and thus restrict PD opening against virus spreading (Fig. 7*C*).

Similar to lipid raft components on PM, the PD membrane also contains a variety of abundant lipids (10), which are segregated into a more tightly packed, liquid-ordered (Lo) phase, in

contrast with the unsaturated lipids that are assembled into a less tightly packed liquid-disordered (Ld) phase (52, 53). Tilsner et al. (54) also proposed that a key attribute of PD architecture is its high degree of membrane curvature, involved in a plastic PD membrane system. REM proteins that were known as the foci of ordered nanodomains (55), are required for structuring of lipid ordered domains. Small Lo domains of 10 to 20 nm form spontaneously with a very short lift-time unless they are stabilized by membrane-anchored proteins (such as REM proteins), which assemble at nanodomains reaching 100 to 200 nm in size (53). Although REM is detectable on PD (Fig. 4*A*), it is not a specific PD-located protein. The PD location of REMs is caused by the enrichment of ordered lipids on the membrane surrounding the PD (10, 25). When REM proteins are incorporated between lipid molecules, they modify the mean size of the ordered domains and increase membrane tension (56). Perraki et al. (37) have demonstrated that potato virus X (*PVX*) infection increased REM1.3 mobility and stimulated bigger nanodomain formation, which is consistent with the phenomenon in our observation that high SA or *CMV* infection promotes REM-labeled nanodomain compartmentalization. REM showed a dynamic and tunable range for protein clustering upon different treated conditions that are suggested by the different steps of bleaching and different intensity from our SIM data. The range of lipid order change could depend on the range of the changing in REM clustering. Therefore, once the overexpressed REM or SA treatment results in REM clustering to a much higher level, a

tough and rigid membrane system is formed to constrict the membrane curvature at the PD neck region. Thus, funnel-shaped PD appear during SA treatment or when REM is overexpressed. mβcd strongly reverts SA or overexpressed REM on lipid order change, and this process requires the control and buffering by REM protein.

Due to the presence of a rigid cell wall, viruses have to exploit existing channels to facilitate their movement into plants. PD are ideal means by which virus can get through the plant cell and serve as gateways for systemic virus movement (57). PD functionality requires the regulations of several reported factors, such as callose, callose binding proteins (PDCBs), and PD localizing proteins (PDLPs) (4, 20), etc. Wang et al. (9) have demonstrated that SA-mediated PD closure is dependent on callose accumulation, which requires the action of PDLP5 protein. Consistently, our study also showed that callose levels are increased on both apical/basal and lateral walls of SA-treated root cells (*SI Appendix*, Fig. S1 *A* and *B*), implying that SA utilizes multiple regulatory components including callose and lipid order to mediated PD gating. However, PDLP5 cannot directly close PD in the absence of SA signaling components (9), and thus a potential unknown regulator is present downstream of PDLP5 to manipulate PD aperture. We identified REM protein in our study fits well with the properties of this unknown regulator, which directly modifies PD structure and is downstream of SA signaling receptors.

PDCB1 is another type of PD-associated protein, which binds callose at PD and preferentially anchors to the sterol and sphingolipid-enriched membrane raft via its GPI motif (20). Thus, the PDCB1 distribution pattern is influenced by callose homeostasis, lipid raft organization, and potentially other unknown factors. Interestingly, we occasionally found that SA increased PDCB1 signal only on the lateral cell sides (*SI Appendix*, Fig. S1 *A–D*), which is similar with but also different from SA-induced callose deposition (*SI Appendix*, Fig. S1 *A* and *B*). Even though PDCB1 localizes at PD due to its callose binding activity (20), PDCB1 protein abundance is not linearly related to callose abundance. Our study showed that PDCB1 and callose begin to appear on the lateral sides under SA treatment; PD were not formed de novo due to the missing unknown factors for PD biogenesis (Fig. 1*C*). Addressing these interesting questions in the near future would deliver more comprehensive understanding of the biogenesis of PD.

Methods

Confocal Microscopy Observation. Images were taken by either Zeiss LSM 880 (with Airyscan) or Leica SP8 confocal microscopes, or 2D-SIM. The settings of excitation and detection were as follows: GFP, 488 nm, 505 to 550 nm; YFP, 488 nm, 495 to 550 nm; aniline blue, 405 nm, 420 to 480 nm; FM4-64, 561 nm, 590 to 760 nm. All images in a single experiment were captured with the same setting. Root meristematic zone of 4-d-old seedlings was consistently used for confocal microscopy observation.

The rest of the protocols used for plant growth, phenotype analysis, cloning, data quantification, etc., are described in *SI Appendix*.

1. T. M. Burch-Smith, S. Stonebloom, M. Xu, P. C. Zambryski, Plasmodesmata during development: Re-examination of the importance of primary, secondary, and branched plasmodesmata structure versus function. *Protoplasma* **248**, 61–74 (2011).
2. A. J. Maule, Plasmodesmata: Structure, function and biogenesis. *Curr. Opin. Plant Biol.* **11**, 680–686 (2008).
3. W. J. Nicolas et al., Architecture and permeability of post-cytokinesis plasmodesmata lacking cytoplasmic sleeves. *Nat. Plants* **3**, 17082 (2017).
4. S. W. Wu, R. Kumar, A. B. B. Iswanto, J. Y. Kim, Callose balancing at plasmodesmata. *J. Exp. Bot.* **69**, 5325–5339 (2018).
5. C. Cheval, C. Faulkner, Plasmodesmal regulation during plant-pathogen interactions. *New Phytol.* **217**, 62–67 (2018).
6. M. Heinlein, Plasmodesmata: Channels for viruses on the move. *Methods Mol. Biol.* **1217**, 25–52 (2015).
7. J. Shah, J. Zeier, Long-distance communication and signal amplification in systemic acquired resistance. *Front. Plant Sci.* **4**, 30 (2013).
8. D. A. Dempsey, D. F. Klessig, SOS—too many signals for systemic acquired resistance? *Trends Plant Sci.* **17**, 538–545 (2012).
9. X. Wang et al., Salicylic acid regulates plasmodesmata closure during innate immune responses in Arabidopsis. *Plant Cell* **25**, 2315–2329 (2013).
10. M. S. Grison et al., Specific membrane lipid composition is important for plasmodesmata function in Arabidopsis. *Plant Cell* **27**, 1228–1250 (2015).
11. K. Jacobson, O. G. Mouritsen, R. G. Anderson, Lipid rafts: At a crossroad between cell biology and physics. *Nat. Cell Biol.* **9**, 7–14 (2007).
12. S. Chiantia, E. London, Sphingolipids and membrane domains: Recent advances. *Handb. Exp. Pharmacol.*, 33–55 (2013).
13. J. Gronnier et al., Structural basis for plant plasma membrane protein dynamics and organization into functional nanodomains. *Elife* **6**, e26404 (2017).
14. S. Raffaele, S. Mongrand, P. Gamas, A. Niebel, T. Ott, Genome-wide annotation of remorins, a plant-specific protein family: Evolutionary and functional perspectives. *Plant Physiol.* **145**, 593–600 (2007).
15. I. K. Jarsch et al., Plasma membranes are subcompartmentalized into a plethora of coexisting and diverse microdomains in Arabidopsis and Nicotiana benthamiana. *Plant Cell* **26**, 1698–1711 (2014).
16. S. S. Konrad et al., S-acylation anchors Remorin proteins to the plasma membrane but does not primarily determine their localization in membrane microdomains. *New Phytol.* **203**, 758–769 (2014).
17. D. Martinez et al., Coiled-coil oligomerization controls localization of the plasma membrane REMORINs. *J. Struct. Biol.* **206**, 12–19 (2019).
18. T. J. Ross-Elliott et al., Phloem unloading in Arabidopsis roots is convective and regulated by the phloem-pole pericycle. *Elife* **6**, e24125 (2017).
19. K. J. Oparka, C. M. Duckett, D. A. M. Prior, D. B. Fisher, Real-time imaging of phloem unloading in the root tip of Arabidopsis. *Plant J.* **6**, 759–766 (1994).
20. C. Simpson, C. Thomas, K. Findlay, E. Bayer, A. J. Maule, An Arabidopsis GPI-anchor plasmodesmal neck protein with callose binding activity and potential to regulate cell-to-cell trafficking. *Plant Cell* **21**, 581–594 (2009).
21. C. Zurzolo, K. Simons, Glycosylphosphatidylinositol-anchored proteins: Membrane organization and transport. *Biochim. Biophys. Acta* **1858**, 632–639 (2016).
22. R. Zavaliev, X. Dong, B. L. Epel, Glycosylphosphatidylinositol (GPI) modification serves as a primary plasmodesmal sorting signal. *Plant Physiol.* **172**, 1061–1073 (2016).
23. M. J. Jaffe, A. C. Leopold, Callose deposition during gravitropism of Zea mays and Pisum sativum and its inhibition by 2-deoxy-D-glucose. *Planta* **161**, 20–26 (1984).
24. A. B. Iswanto, J. Y. Kim, Lipid raft, regulator of plasmodesmal callose homeostasis. *Plants* **6**, 15 (2017).
25. E. Sezgin, I. Levental, S. Mayor, C. Eggeling, The mystery of membrane organization: Composition, regulation and roles of lipid rafts. *Nat. Rev. Mol. Cell Biol.* **18**, 361–374 (2017).
26. L. Jin et al., Characterization and application of a new optical probe for membrane lipid domains. *Biophys. J.* **90**, 2563–2575 (2006).
27. P. Liu et al., Lipid microdomain polarization is required for NADPH oxidase-dependent ROS signaling in Picea meyeri pollen tube tip growth. *Plant J.* **60**, 303–313 (2009).
28. D. M. Owen, C. Rentero, A. Magenau, A. Abu-Siniyeh, K. Gaus, Quantitative imaging of membrane lipid order in cells and organisms. *Nat. Protoc.* **7**, 24–35 (2011).
29. S. H. Spoel et al., Proteasome-mediated turnover of the transcription coactivator NPR1 plays dual roles in regulating plant immunity. *Cell* **137**, 860–872 (2009).
30. Z. Q. Fu et al., NPR3 and NPR4 are receptors for the immune signal salicylic acid in plants. *Nature* **486**, 228–232 (2012).
31. S. Raffaele et al., Remorin, a Solanaceae protein resident in membrane rafts and plasmodesmata, impairs potato virus X movement. *Plant Cell* **21**, 1541–1555 (2009).
32. P. J. Quinn, C. Wolf, The liquid-ordered phase in membranes. *Biochim. Biophys. Acta* **1788**, 33–46 (2009).
33. T. Zhou et al., Domains of the cucumber mosaic virus 2b silencing suppressor protein affecting inhibition of salicylic acid-induced resistance and priming of salicylic acid accumulation during infection. *J. Gen. Virol.* **95**, 1408–1413 (2014).
34. J. L. Cacas et al., Lipids of plant membrane rafts. *Prog. Lipid Res.* **51**, 272–299 (2012).
35. M. D. Curtis, U. Grossniklaus, A gateway cloning vector set for high-throughput functional analysis of genes in planta. *Plant Physiol.* **133**, 462–469 (2003).
36. D. Liang, R. G. White, P. M. Waterhouse, Gene silencing in Arabidopsis spreads from the root to the shoot, through a gating barrier, by template-dependent, nonvascular, cell-to-cell movement. *Plant Physiol.* **159**, 984–1000 (2012).

37. A. Perraki et al., REM1.3's phospho-status defines its plasma membrane nanodomain organization and activity in restricting PVX cell-to-cell movement. PLoS Pathog. 14, e1007378 (2018).

38. H. Chen et al., Firefly luciferase complementation imaging assay for protein-protein interactions in plants. Plant Physiol. 146, 368–376 (2008).

39. S. Sullivan, C. E. Thomson, E. Kaiserli, J. M. Christie, Interaction specificity of Arabidopsis 14-3-3 proteins with phototropin receptor kinases. FEBS Lett. 583, 2187–2193 (2009).

40. K. Prado et al., Oscillating aquaporin phosphorylation and 14-3-3 proteins mediate the circadian regulation of leaf hydraulics. Plant Cell 31, 417–429 (2019).

41. H. Wang et al., Dual role of BKI1 and 14-3-3 s in brassinosteroid signaling to link receptor with transcription factors. Dev. Cell 21, 825–834 (2011).

42. X. Huang et al., Shade-induced nuclear localization of PIF7 is regulated by phosphorylation and 14-3-3 proteins in Arabidopsis. Elife 7, e31636 (2018).

43. H. Ryu et al., Nucleocytoplasmic shuttling of BZR1 mediated by phosphorylation is essential in Arabidopsis brassinosteroid signaling. Plant Cell 19, 2749–2762 (2007).

44. R. Lozano-Durán, S. Robatzek, 14-3-3 proteins in plant-pathogen interactions. Mol. Plant Microbe Interact. 28, 511–518 (2015).

45. F. Giska et al., Phosphorylation of HopQ1, a type III effector from Pseudomonas syringae, creates a binding site for host 14-3-3 proteins. Plant Physiol. 161, 2049–2061 (2013).

46. T. Stanislas et al., Quantitative proteomics reveals a dynamic association of proteins to detergent-resistant membranes upon elicitor signaling in tobacco. Mol. Cell. Proteomics 8, 2186–2198 (2009).

47. J. Keicher et al., Arabidopsis 14-3-3 epsilon members contribute to polarity of PIN auxin carrier and auxin transport-related development. Elife 6, e24336 (2017).

48. J. Tian et al., TRV-GFP: A modified tobacco rattle virus vector for efficient and visualizable analysis of gene function. J. Exp. Bot. 65, 311–322 (2014).

49. S. Mongrand, T. Stanislas, E. M. Bayer, J. Lherminier, F. Simon-Plas, Membrane rafts in plant cells. Trends Plant Sci. 15, 656–663 (2010).

50. F. Simon-Plas, A. Perraki, E. Bayer, P. Gerbeau-Pissot, S. Mongrand, An update on plant membrane rafts. Curr. Opin. Plant Biol. 14, 642–649 (2011).

51. N. A. Eckardt, Membrane rafts and virus movement in plant cells. Plant Cell 21, 1326 (2009).

52. K. Bacia, P. Schwille, T. Kurzchalia, Sterol structure determines the separation of phases and the curvature of the liquid-ordered phase in model membranes. Proc. Natl. Acad. Sci. U.S.A. 102, 3272–3277 (2005).

53. M. Lokar et al., The role of cholesterol-sphingomyelin membrane nanodomains in the stability of intercellular membrane nanotubes. Int. J. Nanomedicine 7, 1891–1902 (2012).

54. J. Tilsner, W. Nicolas, A. Rosado, E. M. Bayer, Staying tight: Plasmodesmal membrane contact sites and the control of cell-to-cell connectivity in plants. Annu. Rev. Plant Biol. 67, 337–364 (2016).

55. I. K. Jarsch, T. Ott, Perspectives on remorin proteins, membrane rafts, and their role during plant-microbe interactions. Mol. Plant Microbe Interact. 24, 7–12 (2011).

56. K. Grosjean et al., Interactions between lipids and proteins are critical for organization of plasma membrane-ordered domains in tobacco BY-2 cells. J. Exp. Bot. 69, 3545–3557 (2018).

57. J. Y. Lee, New and old roles of plasmodesmata in immunity and parallels to tunneling nanotubes. Plant Sci. 221-222, 13–20 (2014).